Search for the Standard Model Higgs Boson at the LEP2 Collider near $\sqrt{s} = 183$ GeV

The ALEPH Collaboration[*])

Abstract

During 1997 the ALEPH experiment at LEP gathered 57 pb^{-1} of data at centre-of-mass energies near 183 GeV. These data are used to look for possible signals from the production of the Standard Model Higgs boson in the reaction $e^+e^- \to HZ$. No evidence of a signal is found in the data; seven events are selected, in agreement with the expectation of 7.2 events from background processes. This observation results in an improved lower limit on the mass of the Higgs boson: $m_H > 87.9$ GeV/c^2 at 95% confidence level.

The ALEPH Collaboration wish to dedicate this paper to
the memory of Colin Raine who died suddenly on September 16, 1998.

Accepted for publication in Physics Letters B

[*]) See next pages for the list of authors

The ALEPH Collaboration

R. Barate, D. Buskulic, D. Decamp, P. Ghez, C. Goy, S. Jezequel, J.-P. Lees, A. Lucotte, F. Martin, E. Merle, M.-N. Minard, J.-Y. Nief, P. Perrodo, B. Pietrzyk

Laboratoire de Physique des Particules (LAPP), IN²P³-CNRS, F-74019 Annecy-le-Vieux Cedex, France

R. Alemany, M.P. Casado, M. Chmeissani, J.M. Crespo, M. Delfino, E. Fernandez, M. Fernandez-Bosman, Ll. Garrido,[15] E. Graugès, A. Juste, M. Martinez, G. Merino, R. Miquel, Ll.M. Mir, P. Morawitz, A. Pacheco, I.C. Park, A. Pascual, I. Riu, F. Sanchez

Institut de Física d'Altes Energies, Universitat Autònoma de Barcelona, 08193 Bellaterra (Barcelona), E-Spain[7]

A. Colaleo, D. Creanza, M. de Palma, G. Gelao, G. Iaselli, G. Maggi, M. Maggi, S. Nuzzo, A. Ranieri, G. Raso, F. Ruggieri, G. Selvaggi, L. Silvestris, P. Tempesta, A. Tricomi,[3] G. Zito

Dipartimento di Fisica, INFN Sezione di Bari, I-70126 Bari, Italy

X. Huang, J. Lin, Q. Ouyang, T. Wang, Y. Xie, R. Xu, S. Xue, J. Zhang, L. Zhang, W. Zhao

Institute of High-Energy Physics, Academia Sinica, Beijing, The People's Republic of China[8]

D. Abbaneo, U. Becker,[22] G. Boix,[24] M. Cattaneo, F. Cerutti, V. Ciulli, G. Dissertori, H. Drevermann, R.W. Forty, M. Frank, F. Gianotti, R. Hagelberg, A.W. Halley, J.B. Hansen, J. Harvey, P. Janot, B. Jost, I. Lehraus, O. Leroy, P. Maley, P. Mato, A. Minten, L. Moneta,[20] A. Moutoussi, F. Ranjard, L. Rolandi, D. Rousseau, D. Schlatter, M. Schmitt,[1] O. Schneider, W. Tejessy, F. Teubert, I.R. Tomalin, E. Tournefier, M. Vreeswijk, H. Wachsmuth

European Laboratory for Particle Physics (CERN), CH-1211 Geneva 23, Switzerland

Z. Ajaltouni, F. Badaud G. Chazelle, O. Deschamps, S. Dessagne, A. Falvard, C. Ferdi, P. Gay, C. Guicheney, P. Henrard, J. Jousset, B. Michel, S. Monteil, J-C. Montret, D. Pallin, P. Perret, F. Podlyski

Laboratoire de Physique Corpusculaire, Université Blaise Pascal, IN²P³-CNRS, Clermont-Ferrand, F-63177 Aubière, France

J.D. Hansen, J.R. Hansen, P.H. Hansen, B.S. Nilsson, B. Rensch, A. Wäänänen

Niels Bohr Institute, 2100 Copenhagen, DK-Denmark[9]

G. Daskalakis, A. Kyriakis, C. Markou, E. Simopoulou, A. Vayaki

Nuclear Research Center Demokritos (NRCD), GR-15310 Attiki, Greece

A. Blondel, J.-C. Brient, F. Machefert, A. Rougé, M. Rumpf, R. Tanaka, A. Valassi,[6] H. Videau

Laboratoire de Physique Nucléaire et des Hautes Energies, Ecole Polytechnique, IN²P³-CNRS, F-91128 Palaiseau Cedex, France

E. Focardi, G. Parrini, K. Zachariadou

Dipartimento di Fisica, Università di Firenze, INFN Sezione di Firenze, I-50125 Firenze, Italy

R. Cavanaugh, M. Corden, C. Georgiopoulos, T. Huehn, D.E. Jaffe

Supercomputer Computations Research Institute, Florida State University, Tallahassee, FL 32306-4052, USA [13,14]

A. Antonelli, G. Bencivenni, G. Bologna,[4] F. Bossi, P. Campana, G. Capon, V. Chiarella, P. Laurelli, G. Mannocchi,[5] F. Murtas, G.P. Murtas, L. Passalacqua, M. Pepe-Altarelli[12]

Laboratori Nazionali dell'INFN (LNF-INFN), I-00044 Frascati, Italy

M. Chalmers, L. Curtis, J.G. Lynch, P. Negus, V. O'Shea, C. Raine, J.M. Scarr, P. Teixeira-Dias, A.S. Thompson, E. Thomson, J.J. Ward

Department of Physics and Astronomy, University of Glasgow, Glasgow G12 8QQ,United Kingdom[10]

O. Buchmüller, S. Dhamotharan, C. Geweniger, P. Hanke, G. Hansper, V. Hepp, E.E. Kluge, A. Putzer, J. Sommer, K. Tittel, S. Werner, M. Wunsch

Institut für Hochenergiephysik, Universität Heidelberg, D-69120 Heidelberg, Germany[16]

R. Beuselinck, D.M. Binnie, W. Cameron, P.J. Dornan,[12] M. Girone, S. Goodsir, N. Marinelli, E.B. Martin, J. Nash, J.K. Sedgbeer, P. Spagnolo, M.D. Williams

Department of Physics, Imperial College, London SW7 2BZ, United Kingdom[10]

V.M. Ghete, P. Girtler, E. Kneringer, D. Kuhn, G. Rudolph

Institut für Experimentalphysik, Universität Innsbruck, A-6020 Innsbruck, Austria[18]

A.P. Betteridge, C.K. Bowdery, P.G. Buck, P. Colrain, G. Crawford, G. Ellis, A.J. Finch, F. Foster, G. Hughes, R.W.L. Jones, A.N. Robertson, M.I. Williams

Department of Physics, University of Lancaster, Lancaster LA1 4YB, United Kingdom[10]

P. van Gemmeren, I. Giehl, C. Hoffmann, K. Jakobs, K. Kleinknecht, M. Kröcker, H.-A. Nürnberger, G. Quast, B. Renk, E. Rohne, H.-G. Sander, S. Schmeling, C. Zeitnitz, T. Ziegler

Institut für Physik, Universität Mainz, D-55099 Mainz, Germany[16]

J.J. Aubert, C. Benchouk, A. Bonissent, J. Carr,[12] P. Coyle, A. Ealet, D. Fouchez, F. Motsch, P. Payre, M. Talby, M. Thulasidas, A. Tilquin

Centre de Physique des Particules, Faculté des Sciences de Luminy, IN^{2}P^3-CNRS, F-13288 Marseille, France

M. Aleppo, M. Antonelli, F. Ragusa

Dipartimento di Fisica, Università di Milano e INFN Sezione di Milano, I-20133 Milano, Italy.

R. Berlich, V. Büscher, H. Dietl, G. Ganis, K. Hüttmann, G. Lütjens, C. Mannert, W. Männer, H.-G. Moser, S. Schael, R. Settles, H. Seywerd, H. Stenzel, W. Wiedenmann, G. Wolf

Max-Planck-Institut für Physik, Werner-Heisenberg-Institut, D-80805 München, Germany[16]

J. Boucrot, O. Callot, S. Chen, M. Davier, L. Duflot, J.-F. Grivaz, Ph. Heusse, A. Höcker, A. Jacholkowska, M. Kado, D.W. Kim,[2] F. Le Diberder, J. Lefrançois, L. Serin, J.-J. Veillet, I. Videau,[12] J.-B. de Vivie de Régie, D. Zerwas

Laboratoire de l'Accélérateur Linéaire, Université de Paris-Sud, IN^{2}P^3-CNRS, F-91898 Orsay Cedex, France

P. Azzurri, G. Bagliesi,[12] S. Bettarini, T. Boccali, C. Bozzi, G. Calderini, R. Dell'Orso, R. Fantechi, I. Ferrante, A. Giassi, A. Gregorio, F. Ligabue, A. Lusiani, P.S. Marrocchesi, A. Messineo, F. Palla, G. Rizzo, G. Sanguinetti, A. Sciabà, G. Sguazzoni, R. Tenchini, C. Vannini, A. Venturi, P.G. Verdini

Dipartimento di Fisica dell'Università, INFN Sezione di Pisa, e Scuola Normale Superiore, I-56010 Pisa, Italy

G.A. Blair, J.T. Chambers, J. Coles, G. Cowan, M.G. Green, T. Medcalf, J.A. Strong, J.H. von Wimmersperg-Toeller

Department of Physics, Royal Holloway & Bedford New College, University of London, Surrey TW20 OEX, United Kingdom[10]

D.R. Botterill, R.W. Clifft, T.R. Edgecock, P.R. Norton, J.C. Thompson, A.E. Wright

Particle Physics Dept., Rutherford Appleton Laboratory, Chilton, Didcot, Oxon OX11 OQX, United Kingdom[10]

B. Bloch-Devaux, P. Colas, B. Fabbro, G. Faïf, E. Lançon,[12] M.-C. Lemaire, E. Locci, P. Perez, H. Przysiezniak, J. Rander, J.-F. Renardy, A. Rosowsky, A. Trabelsi,[23] B. Tuchming, B. Vallage

CEA, DAPNIA/Service de Physique des Particules, CE-Saclay, F-91191 Gif-sur-Yvette Cedex, France[17]

S.N. Black, J.H. Dann, H.Y. Kim, N. Konstantinidis, A.M. Litke, M.A. McNeil, G. Taylor

Institute for Particle Physics, University of California at Santa Cruz, Santa Cruz, CA 95064, USA[19]

C.N. Booth, S. Cartwright, F. Combley, M.S. Kelly, M. Lehto, L.F. Thompson

Department of Physics, University of Sheffield, Sheffield S3 7RH, United Kingdom[10]

K. Affholderbach, A. Böhrer, S. Brandt, J. Foss, C. Grupen, G. Prange, L. Smolik, F. Stephan

Fachbereich Physik, Universität Siegen, D-57068 Siegen, Germany[16]

G. Giannini, B. Gobbo

Dipartimento di Fisica, Università di Trieste e INFN Sezione di Trieste, I-34127 Trieste, Italy

J. Putz, J. Rothberg, S. Wasserbaech, R.W. Williams

Experimental Elementary Particle Physics, University of Washington, WA 98195 Seattle, U.S.A.

S.R. Armstrong, E. Charles, P. Elmer, D.P.S. Ferguson, Y. Gao, S. González, T.C. Greening, O.J. Hayes, H. Hu, S. Jin, G. Mamier, P.A. McNamara III, J.M. Nachtman,[21] J. Nielsen, W. Orejudos, Y.B. Pan, Y. Saadi, I.J. Scott, M. Vogt, J. Walsh, Sau Lan Wu, X. Wu, G. Zobernig

Department of Physics, University of Wisconsin, Madison, WI 53706, USA[11]

1 Introduction

The Standard Model is very successful in describing the interactions of elementary particles. However, the origin of the particle masses remains an open question. The Higgs mechanism directly addresses this problem, with the $W^{\pm}$ and Z gauge bosons acquiring mass via spontaneous symmetry breaking. A consequence of the Higgs mechanism is the addition of a neutral scalar particle, the Higgs boson, to the spectrum of elementary particles. While the Higgs boson mass m_H is not predicted by the theory, recent results of fits to experimental electroweak data favour low mass values [1].

At LEP2, the Higgs boson can be produced through the Higgs-strahlung process, $e^+e^- \to HZ$, with smaller contributions to the $H\nu\bar{\nu}$ and He^+e^- channels from W- and Z-fusion processes. In the Standard Model, the Higgs boson production rate and decay branching ratios are calculable as a function of m_H [2]. In the mass region relevant to LEP2 searches, the Higgs boson decays mostly into $b\bar{b}$ and, to a lesser extent, into $\tau^+\tau^-$. The searches described in this paper cover most of the topologies arising from the HZ process, with $H \to$ hadrons or $\tau^+\tau^-$, and $Z \to e^+e^-, \mu^+\mu^-, \tau^+\tau^-, \nu\bar{\nu}$, or $q\bar{q}$.

The LEP collider has been operating at centre-of-mass energies above the W^+W^- production threshold since 1996. The ALEPH Collaboration has searched for the Higgs boson with ~ 20 pb^{-1} of data accumulated at $\sqrt{s} = 161$ and 170–172 GeV: no evidence of a signal was detected, and a lower limit of 70.7 GeV/c^2 at 95% confidence level was set on the Higgs boson mass [3]. The other three LEP experiments have reported similar results [4, 5, 6].

A total integrated luminosity of 57 pb^{-1} was accumulated by ALEPH in 1997 at centre-of-mass energies near 183 GeV: 0.2 pb^{-1} at 180.8 GeV, 3.9 pb^{-1} at 181.7 GeV, 51.0 pb^{-1} at 182.7 GeV, and 1.9 pb^{-1} at 183.8 GeV. In this letter, these data are referred to as "the 183 GeV data." The higher centre-of-mass energies and the larger total luminosity increase the experimental detection sensitivity for the Higgs boson to a mass around 85 GeV/c^2. Therefore a reference signal with $m_H = 85$ GeV/c^2 and $\sqrt{s} = 183$ GeV is used when optimizing the event selections and quoting signal detection efficiencies. The total production cross section for the reference signal is 0.37 pb.

To improve the discriminating power between signal and background processes, the previously published selections [3] are updated, and new event selections based on artificial neural networks are introduced. Another new feature of Higgs boson searches at $\sqrt{s} \sim 183$ GeV is the higher and partly irreducible ZZ background; since these centre-of-mass energies lie on the threshold for ZZ production, a significant fraction of these events have only one on-shell Z boson.

This letter is organized in the following manner. Section 2 provides a brief description of the ALEPH detector and the b-tagging scheme used in the searches. An overview of the search strategy and of the method used to combine the event selections in all the channels is presented in Section 3. The event selection criteria for each of the signal final states are described in Sections 4.1 through 4.4; new developments with respect to the previous publications [3, 7] are emphasized and systematic uncertainties specific to each channel are also summarized. In Section 5 the combination of all search channels is presented and the final result is derived. A summary follows in Section 6.

2 The ALEPH detector

In this section the ALEPH detector parts which are most relevant for the analyses that follow are succinctly described. A more comprehensive description of the detector and its performance is given in Refs. [8] and [9].

Three coaxial tracking devices surround the beam line. The innermost device is a silicon microstrip vertex detector (VDET) [10]. It consists of two cylindrical layers of silicon wafers situated at average radii of 6.3 and 11.0 cm. Charged particles with polar angle in the range $|\cos\theta| < 0.88$ traverse both VDET layers. The VDET is surrounded by a 2 m long inner tracking wire chamber (ITC) which provides up to eight hits between radii of 16 and 26 cm. Outside of the ITC is the main tracking detector, a large time projection chamber (TPC) which measures up to 21 three-dimensional coordinates per charged particle. The TPC also measures up to 338 samples of the specific energy loss per track, allowing charged particle identification. A superconducting solenoid immerses the central tracking volume in a 1.5 T axial magnetic field.

In this letter, charged particle tracks reconstructed with at least four hits in the TPC and which originate from within a cylinder of 2 cm radius and 20 cm length centred on the nominal interaction point are called *good tracks*. The tracking ensemble achieves a momentum resolution $\sigma(p_t)/p_t$ of 6×10^{-4} $(\mathrm{GeV}/c)^{-1}$ $p_t \oplus 0.005$. The three-dimensional resolution on the impact parameter of tracks can be parameterized as $(34 + 70/p) \times (1 + 1.6\cos^4\theta)$ μm, with p in GeV/c.

The precise measurement of track parameters plays an essential rôle in the identification of jets containing b hadrons. Weakly decaying b hadrons are long-lived, typically flying several millimetres before decaying. The tagging of b-quark jets relies on six variables reflecting the impact parameter of tracks in the jet, reconstructed secondary vertices, identified electrons and muons with large transverse momentum with respect to the jet axis, and jet shape and multiplicity variables. A neural network is used to combine this information into an output η for each jet. The network is trained to have a response near zero for light quark jets and near one for b quark jets [7].

A lead/proportional-chamber electromagnetic calorimeter (ECAL) is also situated inside the superconducting coil. It is finely segmented into projective towers of $0.9° \times 0.9°$, allowing the identification of electrons and photons within jets. Luminosity calorimeters are installed between the ECAL endcaps and the beam pipe. These calorimeters are of similar construction to ECAL and are treated as an extension of it. A relative energy resolution of $0.18/\sqrt{E(\mathrm{GeV})} + 0.009$ is achieved. A silicon-tungsten sampling calorimeter completes the electromagnetic calorimeter coverage down to 34 mrad.

The ECAL is surrounded by a hadron calorimeter (HCAL) consisting of 5 cm thick iron slabs instrumented with streamer tubes; this structure serves as the return yoke for the magnetic field. The HCAL has the dual purpose of measuring hadronic energy deposition as well as acting as a filter for the identification of muons. When used in conjunction with the ECAL, a relative energy resolution of $0.85/\sqrt{E(\mathrm{GeV})}$ is achieved for hadrons. The outermost detectors are two double layers of muon chambers. Muons are identified as charged particles which penetrate the whole depth of the HCAL or which have associated hits in the outer chambers.

The measurements of charged particle tracks and of energy deposition in the calorimeters, combined with the identification of photons, electrons, and muons, are used to produce a list

of charged and neutral *energy flow particles* which are used in all the analyses which follow. Hadronic jets are clustered from these objects with a resolution approximately described as $\sigma(E) = (0.60\sqrt{E} + 0.6)$ GeV $\times (1 + \cos^2\theta)$, where E is the jet energy in GeV and θ is its polar angle. The resolution on the jet angles is approximately 20 mrad in both θ and ϕ.

The total uncertainty on the integrated luminosity of the accumulated data is less than 0.6%.

3   Search strategy

Event selections have been previously developed [3] for the various topologies arising from the HZ process. These selections address the H$\ell^+\ell^-$ channel (here and in the following, ℓ denotes an electron or a muon, collectively referred to as "leptons"), the H$\nu\bar{\nu}$ channel, the H$q\bar{q}$ channel where H $\to \tau^+\tau^-$ decays are not included, the H$\tau^+\tau^-$ channel, and the $\tau^+\tau^-q\bar{q}$ channel which complements the H$q\bar{q}$ channel when H decays to a $\tau^+\tau^-$ pair. These selections are reoptimized for the increased centre-of-mass energy and integrated luminosity and are supplemented with new event selections. In the H$\ell^+\ell^-$ final state the selection is improved to extend the acceptance into an angular region not considered previously. In final states with τ leptons, the previous track-based τ candidate selection is replaced by a minijet-based selection, and the previous cut-based event selection algorithms are replaced with new selections based upon neural network (NN) combinations of discriminating variables. In the H$\nu\bar{\nu}$ and the H$q\bar{q}$ channels, new NN-based event selections complement the published cut-based selections [3].

The various selections are optimized to maximize the sensitivity to a Higgs boson signal with mass 85 GeV/c^2, which is near the expected experimental sensitivity. The expected combined confidence level on the signal hypothesis that would be obtained on average if no signal were present [11] is minimized with respect to the position of the cuts on the most relevant selection variables:

- the reconstructed Z mass in the H$\ell^+\ell^-$ selection;

- the b-quark content of the event and the event acoplanarity in the H$\nu\bar{\nu}$ cut-based selection;

- the b-quark content of the jets from a candidate Higgs boson and the invariant mass of jets from the Z boson in the H$q\bar{q}$ cut-based selection;

- the neural network outputs in the H$\nu\bar{\nu}$ and the H$q\bar{q}$ neural network selections, and in the H$\tau^+\tau^-$ and $\tau^+\tau^-q\bar{q}$ selections.

The confidence level for each channel is computed without performing any background subtraction. All channels are subsequently combined using the elitist prescription described in Ref. [11]. This combination prescription assigns different weights to the various search channels in an optimal manner according to their sensitivities to the signal hypothesis.

When two selections are available for a given final state, their results are combined instead of keeping only the selection leading to the (often marginally) better expected confidence level. The gain from this combination procedure is significant since, when two analyses are aimed at selecting the same signal and have similar performance, they often have a large overlap in signal efficiency but not so large an overlap in terms of background. Signal events are, unlike

reducible background events, signal-like in *many* variables. The selection of a background event by both selections is therefore less probable, as it depends on the specific choice of variables in each of the selections. The two four-jet final state selections illustrate this point, as is summarized in Table 1. The two original selections are therefore separated into three

Table 1: Signal efficiency and the number of signal and background events expected to be selected by each of two four-jet event selections (cuts and neural network), by the two selections simultaneously, and by each of the two exclusively. In this table the selection criteria of the cut-based and neural network selections are optimized independently of one another, and together with all other channels.

Selection	Efficiency (%)	Signal	Background
NN	25.7	3.53	1.50
Cuts	24.1	3.31	1.48
Cuts and NN	19.8	2.72	0.88
Cuts only	4.3	0.59	0.60
NN only	5.9	0.81	0.62
Total	30.0	4.12	2.10

statistically independent and thus easily combinable sub-selections. The first sub-selection, corresponding to the overlap of the two original analyses, is very pure. The two less pure exclusive selections contain additional information and are combined with the first, decreasing further the overall expected confidence level. The combination of the three sub-selections is also done with the elitist prescription. As a result, the events selected by both original analyses receive a larger weight (being more signal-like) than those selected exclusively by one of the two (being more background-like).

Systematic uncertainties related to the knowledge of the residual background shape and normalization do not affect the results presented in this letter since no background subtraction is performed. As is also the case in Ref. [3], the reconstructed Higgs boson mass for all final states is a discriminating variable entering the calculation of the confidence levels. Here, the power of the confidence levels determined from the various searches is improved by including more discriminating variables in the test statistic. These new variables are

- the b content of the event in the $H\nu\bar{\nu}$ channel for the cut-based selection;

- the neural network output in the $H\nu\bar{\nu}$ channel for the NN selection;

- the b content of the hadronic jets for the $H\ell^+\ell^-$ channel.

A global optimization is performed in the manner described above with the criteria of the two $Hq\bar{q}$, the two $H\nu\bar{\nu}$, the $H\ell^+\ell^-$, and the $\tau^+\tau^- q\bar{q}$ and $H\tau^+\tau^-$ selections varied simultaneously. The final sets of selection cuts, leading to the overall smallest expected combined confidence level for $m_H = 85$ GeV/c^2, are described in the following section.

4

Table 2: Signal detection efficiencies (in percent) for different Higgs boson mass values. For the Hq$\bar{\text{q}}$ and H$\nu\bar{\nu}$ channels three independent sub-selections are used: events selected by both the cut-based and the neural network-based selections, and events selected exclusively by either of them. The number of expected background events (n_{b}), the number of events selected in the data (n_{obs}), and the number of expected signal events for $m_{\text{H}} = 85$ GeV/c^2 (n_{s}) are also given.

m_{H} (GeV/c^2)	H$\ell^+\ell^-$	H$\nu\bar{\nu}$			Hq$\bar{\text{q}}$			H$\tau^+\tau^-$	$\tau^+\tau^-$q$\bar{\text{q}}$
		Cuts+NN	Cuts	NN	Cuts+NN	Cuts	NN		
60	79.6	8.8	8.7	4.7	9.3	5.4	8.1	18.1	0.93
70	77.8	15.8	4.4	7.9	12.4	8.6	9.0	22.9	2.9
80	78.3	20.9	2.8	10.9	23.5	7.4	5.2	22.7	9.8
85	76.2	17.9	4.0	12.2	26.1	7.8	5.2	20.7	12.6
90	71.9	11.1	5.2	7.0	24.6	9.4	4.6	17.4	13.6
95	31.1	9.5	2.6	7.2	19.1	7.6	6.0	12.7	11.6
100	4.0	6.0	1.7	5.7	14.2	6.6	6.9	6.8	5.7
Numbers of events									
n_{b}	2.0	0.16	0.08	0.18	1.4	2.1	1.00	0.17	0.16
n_{obs}	3	0	0	0	1	2	1	0	0
n_{s}	1.1	0.82	0.18	0.56	3.6	1.1	0.71	0.14	0.16

4 Event selections

In addition to the cut-based analyses described below, NN-based analyses are introduced for the Hq$\bar{\text{q}}$, H$\nu\bar{\nu}$, H$\tau^+\tau^-$ and $\tau^+\tau^-$q$\bar{\text{q}}$ channels to enhance the event selection performance. Variables which alone show marginal separation between signal and background and would be difficult to incorporate into a cut-based analysis can be effectively used in the neural network framework [12].

In the following subsections, the distributions of simulated background processes are normalized to the collected integrated luminosity, and the distributions of the simulated signal are for a Higgs boson mass of 85 GeV/c^2. The background processes were simulated as described in Ref. [3], with sample sizes typically exceeding the collected data luminosity by a factor $\sim$100. Samples of 10 000 signal events are simulated at several Higgs boson mass values using the HZHA program [13]. In the case of the H$\nu\bar{\nu}$ final state, the W-fusion process as well as its interference with the Higgs-strahlung process are taken into account. Independent training and performance evaluation samples are used for the neural network selections.

The selection efficiencies quoted in this letter are always calculated as the fraction of events in the given channel that pass the selection cuts. Table 2 shows, for each event selection, the variation of efficiency for several Higgs boson masses as well as the expected number of signal events for $m_{\text{H}} = 85$ GeV/c^2, the expected number of background events and the number of events selected in the data.

Although the selections differ between the various analyses, they share common systematic uncertainties. For the Hq$\bar{\text{q}}$, H$\nu\bar{\nu}$, and H$\tau^+\tau^-$ analyses these common systematic effects relate to the tagging of b-quark jets. Systematic effects related to the simulation of track reconstruction

and to the modelling of b-hadron physics are the dominant source of uncertainty in both the cut-based and NN-based analyses. The systematic effect arising from the uncertainty on the b-quark fragmentation hardness (modelled with the Peterson function [14]) is determined by reweighting signal events to cover the experimental uncertainty on the parameter $\epsilon_b = 0.0045 \pm 0.0014$ [15]. Differences in the b-hadron lifetimes and decay multiplicities between the simulation and the world averages are also incorporated in the systematic uncertainty. The uncertainty due to the modelling of the detector tracking is estimated by varying track parameters in accordance with the experimentally measured resolution.

Systematic effects from possible uncertainties in the simulation of the non-b-tagging selection variables are estimated by recomputing the detection efficiency with reweighted signal event samples. The weights are determined from a direct comparison of data and simulated background event distributions at a preselection level with suitably large statistics. Further studies of systematic uncertainties specific to each selection are given below in the corresponding sections.

4.1 The leptonic final states

The H$\ell^+\ell^-$ channel represents 6.7% of the Higgs-strahlung cross section. The signal events are characterized by two leptons with an invariant mass close to m_Z and a recoil mass equal to the Higgs boson mass. Although the branching ratio of this channel is small, the experimental signature is very clear and the Higgs boson mass can be reconstructed with high resolution.

The event selection follows closely that of Ref. [3]. To be considered as lepton candidates charged particles must either be identified as electrons or muons, or else must be isolated from other particles by more than $10°$. All accepted combinations of oppositely charged lepton candidates must have at least one identified lepton. Mixed e-μ pairs are not considered. Final state radiation photons from the Z boson decay products are identified and added to isolated lepton candidates to improve the Higgs boson mass resolution.

The analysis algorithm has been simplified with respect to [3] regarding the treatment of events with only one identified lepton. In such cases, the requirement on the angles of the tracks closest to the lepton candidates as well as the requirement that both lepton candidates be isolated have been dropped.

The definition of lepton candidates has been improved with respect to [3] to include leptons below the main tracking acceptance of $|\cos\theta| \leq 0.95$. Low angle muons are identified down to $7.5°$ from the beam line by finding hit patterns in the hadronic calorimeter consistent with a muon. The momentum of such a low angle muon is calculated from an over-constrained fit to the event using energy and momentum conservation. Low angle electrons are identified down to $12.4°$ from the beam line by finding large isolated energy deposits in the electromagnetic calorimeters. To separate these electrons from photons, an electron candidate must have at least two consistent hits in the ITC. The new definition of lepton candidates improves the H$\ell^+\ell^-$ signal efficiency by approximately 4% for the same purity.

The selection criteria remain unchanged with respect to those published in Ref. [3] with the sole exception of the requirement on the reconstructed Z boson mass which is reoptimized from $m_{\ell^+\ell^-(\gamma)} > 80$ GeV/c^2 to $m_{\ell^+\ell^-(\gamma)} > 82.75$ GeV/c^2.

4.1.1 Systematic uncertainties

Several potential sources of systematic uncertainty are investigated. These include the identification of electrons and muons, the isolation criterion, and the simulation of the energy and momentum resolution of jets and leptons [3]. Some limitations are found in the simulation of the background to low angle electrons which, however, do not contribute any systematic effect. The total relative systematic uncertainty in the signal detection efficiency is 0.4%.

4.2 The missing energy final state

The HZ signal where the Z boson decays invisibly to two neutrinos constitutes 20% of the total Higgs-strahlung cross section. A large missing mass and two b jets from the Higgs boson decay characterize this final state. Two independent analyses are used to search for a signal in this final state: a cut-based analysis modelled on the previous selection [3] and an analysis based on a neural network.

Both analyses share a common hadronic event preselection. The plane perpendicular to the thrust axis is used to divide the event into two hemispheres. All energy flow particles in a hemisphere are considered to belong to a jet, and both jets are required to have nonzero energy. To reduce background from $\gamma\gamma$ interactions, the preselection requires either $P_{\rm t} > 5\%\sqrt{s}$ or $m_{\rm vis} > 30\%\sqrt{s}$, where $P_{\rm t}$ is the total transverse momentum of the event and $m_{\rm vis}$ is the visible mass. Finally, the missing mass of the event must be larger than 80 GeV/c^2.

4.2.1 Event selection with cuts

In order to reject radiative returns to the Z, the missing momentum vector is required to point into the apparatus ($\theta_{p\!\!\!/} > 20°$), and its component along the beam line is not allowed to be large ($|p_{\rm z}| < 26$ GeV/c). The event acoplanarity [3] is used to reduce further the contamination from radiative return events ($\tilde{A} > 0.13$). The energy deposited within a 12° cone around the beam axis is required to be small ($E_{12} < 1.2\%\sqrt{s}$) to reject W$e\nu$ and Zee events with an energetic electron deflected at a low angle into the detector. In order to suppress background from W$^+$W$^- \to$ q$\bar{\rm q}'\tau\nu$ decays, the whole event is reclustered into τ minijets [3], and the most isolated jet is required to have a low energy ($E_\tau < 7$ GeV). Finally, b-tagging information from the jets (Fig. 1a) is used to enhance the signal-to-background ratio ($\eta_1 + \eta_2 > 1.1$).

4.2.2 Event selection with a neural network

The analysis described above is complemented with a neural network selection using the six variables of the cut selection and five additional ones. The new variables include the fraction of the energy deposited beyond 30° of the beam line, the total energy within a 30° azimuthal wedge around the missing momentum direction, the acollinearity of the jets, and an additional combination of the b-tagging variables, $\log_{10}(1 - \eta_1\eta_2/2)$. Finally, the isolation angle of the most isolated track (with $p > 1$ GeV/c) provides additional discriminating power against W$^+$W$^- \to$ q$\bar{\rm q}'\tau\nu$ background.

Further details of the H$\nu\bar{\nu}$ neural network are discussed in the Appendix. Figure 1b shows the neural network output. Events are selected if the neural network response exceeds 0.983.
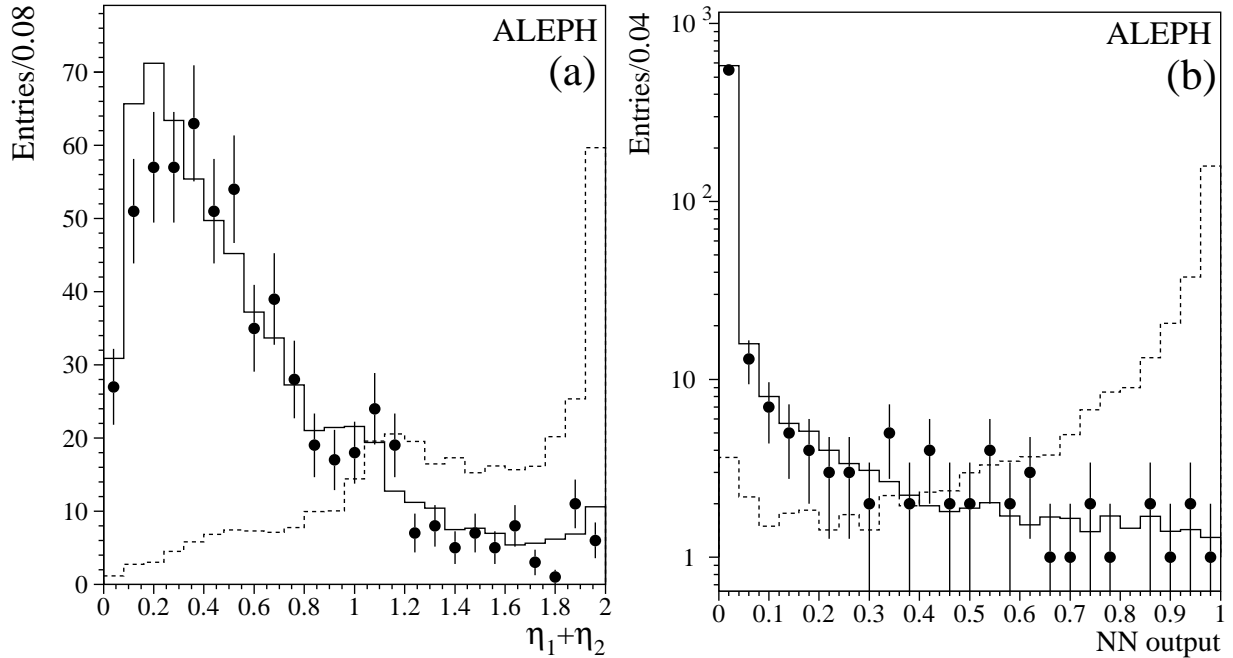
Figure 1: The distributions in the missing energy channel of (a) the sum of the two neural network b-tag outputs and (b) the output of the neural network used for event selection. The distributions are shown for the data (points), the total simulated background (solid histogram) and the reference signal sample (dashed histogram) after the preselection cuts. The signal distributions have an arbitrary normalization.

4.2.3   Systematic uncertainties

Based on deviations between data and Monte Carlo simulation of the kinematic variable distributions, a relative systematic uncertainty of 2.4% on the signal efficiency is determined. The events from Monte Carlo simulation of the HZ signal are reweighted to simulate changes in b fragmentation, lifetime, and decay multiplicity, giving a relative systematic uncertainty of 3.0%. The relative systematic uncertainty from discrepancies between the tracking in the simulated data and real data is 6.1%. The total relative systematic uncertainty on the signal selection efficiency is 7.2%.

4.3   The four-jet final state

Although the $b\bar{b}q\bar{q}$ final state is not as distinctive as the leptonic and missing energy final states, its large branching ratio, 64.4%, compensates for this drawback. The dominant background processes $e^+e^- \rightarrow q\bar{q}$, W^+W^-, ZZ are reduced using event topology, kinematic criteria, and b-tagging information. Two analyses are used to search for this final state: a cut-based analysis [3] and a neural network based analysis.

Common event preselection criteria are used for both the cut-based and neural network analyses. Events are required to have at least eight good tracks satisfying $|\cos\theta| \leq 0.95$. Radiative returns to the Z resonance are rejected when the initial state photon is observed in the apparatus as well as when it escapes down the beam pipe. The events are then forced to form four jets with the Durham jet-clustering algorithm [16]. The y_{cut} value where the

transition from four to three jets occurs (y_{34}) must be larger than 0.004. Each jet is required to contain at least one good track. The energies and masses of the four jets are then rescaled in accordance with energy and momentum conservation. The measured jet velocities are preserved in this process.

4.3.1 Event selection with cuts

The analysis algorithm and the selection criteria are identical to those found in [3] except where explicitly stated otherwise.

The sum Θ of the four smallest interjet angles in the event (Fig. 2a) must be larger than $350°$; this significantly reduces the background contribution from $q\bar{q}$ events where an energetic jet recoils against three softer jets. Since the sensitivity of this analysis approaches the HZ kinematic limit, signal events are expected to have two nearly back-to-back pairs of jets. This event topology is selected by requiring $\gamma = \min(\cos\theta_{ij} + \cos\theta_{kl}) < -1.30$, where the minimum is over all possible $ijkl$ jet permutations.
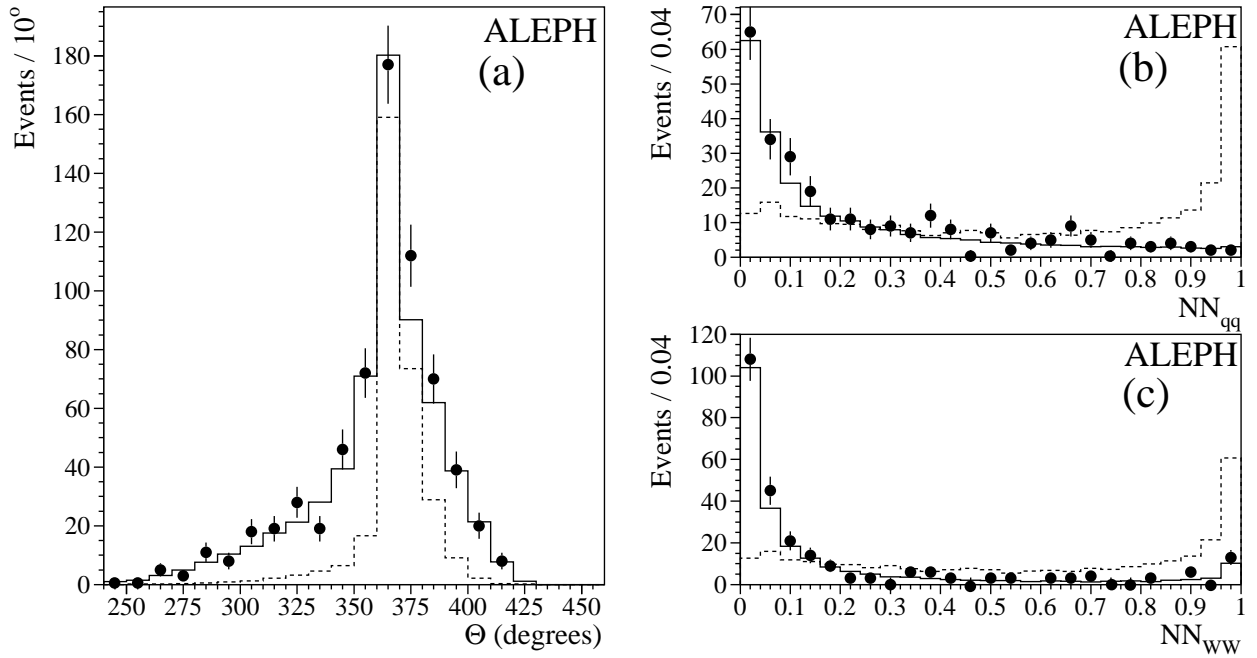

Figure 2: The four-jet channel distributions for preselected events of (a) Θ, and of the outputs of (b) the anti-$q\bar{q}$ and (c) anti-W^+W^- neural networks. The points are the data and the solid histogram is the simulated total background normalized to the data integrated luminosity. The signal distributions (dashed histograms) are shown with an arbitrary normalization.

Further event selection criteria are based upon the six possible jet-pairing combinations. An event is selected if at least one of the jet-pairing combinations conforms to either one of the two following sets of criteria (labelled a and b).

For the first case, events with four well-isolated jets are required. One di-jet system is required to have an invariant mass consistent with the Z mass. The other di-jet is required to have an invariant mass within the Higgs boson mass range of interest and also to have well b-tagged jets. Hence the selection criteria are the following:

a)
- $y_{34} > 0.008$;
- $m_{12} > 78$ GeV/c^2 (Z candidate jets);
- $m_{34} > 55$ GeV/c^2 (Higgs candidate jets);
- $\min(\eta_3, \eta_4) > 0.30$ (Higgs candidate jets);
- $(1 - \eta_3)(1 - \eta_4) < 6 \times 10^{-3}$ (Higgs candidate jets).

Selection criteria for the second case are designed for the HZ $\rightarrow$ b$\bar{\text{b}}$b$\bar{\text{b}}$ final state. These events are almost background free and are selected by requiring that the event as a whole has a high b-quark content and a clear four-jet structure:

b) $9.5 y_{34} + \sum_{i=1}^{4} \eta_i > 2.90$.

4.3.2   Event selection with neural networks

Two neural networks are trained to identify the HZ $\rightarrow$ b$\bar{\text{b}}$q$\bar{\text{q}}$ signal while rejecting the q$\bar{\text{q}}$ and W$^+$W$^-$ backgrounds: one network is specifically designed to reject q$\bar{\text{q}}$ events, while the other is designed to reject W$^+$W$^-$ events. Details related to the training of the neural networks are discussed in the Appendix.

The input patterns to the neural networks consist of the different di-jet pairing combinations within each event. Only pairings that survive the preselection criteria described in Section 4.3 as well as the requirements $\sum_{i=1}^{4} \eta_i > 1.0$ and $m_{34} > 45$ GeV/c^2 are input to the neural networks.

The inputs for both neural networks include several of the selection variables used in the cut-based selection: y_{34}, γ, m_{12}, $\min(\eta_3, \eta_4)$, $(1 - \eta_3)(1 - \eta_4)$, and $\sum_{i=1}^{4} \eta_i$. The invariant mass of the Higgs candidate jets m_{34} is not included to avoid biasing the selection efficiency towards the signal mass hypotheses used for training.

The average QCD four-jet matrix element squared [17] and Θ are especially powerful discriminating variables for eliminating q$\bar{\text{q}}$ background events and hence are also used as inputs to the anti-q$\bar{\text{q}}$ neural network. A vast majority of four-jet events from e$^+$e$^- \rightarrow$ q$\bar{\text{q}}$ are q$\bar{\text{q}}$gg. The following observables offer additional discriminating power between light quark and gluon jets and are included as inputs to the anti-q$\bar{\text{q}}$ neural network: the boosted aplanarity and the boosted sphericity (both calculated in the rest frame of the jet), and the multiplicity of tracks with large rapidity with respect to the jet axis, for the two Z candidate jets. Additional kinematic variables (*e.g.*, jet energies and di-jet masses, smallest interjet angle and angle of the missing momentum with respect to the beam axis) are also included to improve the overall discriminating power. The complete list of input variables for the anti-q$\bar{\text{q}}$ neural network is given in the Appendix.

Important characteristics of W$^+$W$^-$ events compared to HZ $\rightarrow$ b$\bar{\text{b}}$q$\bar{\text{q}}$ signal events include the lack of b jet production and the comparative abundance of c jets. In order to exploit these differences, the common neural network input variables listed above are complemented with the b-tagging information from the two Z candidate jets (η_1 and η_2) and with charm rejection variables for the Higgs candidate jets (μ_3 and μ_4). The charm rejection variables are computed in a similar way to the track impact-parameter-based uds-jet probability P_{jet} [7] but using only tracks with low rapidity with respect to the jet axis ($y < 4.9$) [18]. This rapidity criterion is effective since charmed meson decays result in particles with transverse momentum lower than those from b-hadron decays. The lowest di-jet mass, the lowest jet energy in the event, and the

event broadening variable (defined in the Appendix) are also used. The complete list of input variables for the anti-W^+W^- neural network is given in the Appendix.

The neural network output distributions are shown in Figs. 2b and 2c for signal, background, and data. An event is selected when at least one of its jet pairing combinations has neural network outputs which satisfy both $NN_{q\bar{q}} > 0.940$ and $NN_{W^+W^-} > 0.964$.

4.3.3 Systematic uncertainties

The systematic uncertainties affecting the signal detection efficiency are determined using the method outlined in Section 4. The relative uncertainty from b tagging is 6.5%. The systematic uncertainty corresponding to possible limitations in the description of the most important non-b-tagging selection variables ($y_{34}, \gamma, \Theta, m_{12}, m_{34}, NN_{q\bar{q}}$, and $NN_{W^+W^-}$) is determined to be 2.5%. Conservatively increasing the jet angular resolution in θ and ϕ by 10% in the Monte Carlo simulation results in an additional uncertainty of 0.8%. The correlations between all pairs of variables used in each of the neural networks are compared between the data and the simulated background event sample used for training; no significant discrepancies are observed.

Adding the above contributions in quadrature, the total relative systematic uncertainty assigned to the signal detection efficiency is 7.0%.

4.4 The final states with τ leptons

Two signal channels contribute to final states with at least one $\tau^+\tau^-$ pair. The process $HZ \to H\tau^+\tau^-$ corresponds to 3.4% of the total Higgs-strahlung process, and $H \to \tau^+\tau^-, Z \to q\bar{q}$ corresponds to an additional 5.5%. These events are expected to have two oppositely charged low multiplicity jets in association with missing energy from the τ decays. The main background processes are ZZ and W^+W^-.

Multihadronic events are selected by requiring at least eight good tracks. The total charged track energy in the event is required to exceed 20% of the centre-of-mass energy.

Events from radiative returns to the Z peak, $q\bar{q}(\gamma)$, are rejected with the requirement $|P_z| + E_{\text{miss}} < 1.8\gamma_{\text{peak}}$. Here, P_z and E_{miss} are the total longitudinal momentum of the event and its missing energy. The mean of the initial state radiation (ISR) photon spectrum peak is denoted as γ_{peak} and is defined as $\gamma_{\text{peak}} = \sqrt{s}/2 - m_Z^2/2\sqrt{s}$. In addition, $|P_z|$ is required not to exceed $0.6\gamma_{\text{peak}}$. In order to exploit the missing energy expected in this final state, the total missing transverse momentum of the event is required to be at least $2.5\%\sqrt{s}$.

A new method for identifying τ lepton candidates replaces the previously published track-based approach [3]. The event is clustered into a large number of jets, referred to as *minijets*, with mass consistent with m_τ. The τ candidates are then selected from these minijets according to the procedure described in detail in [19]. This minijet method offers a performance similar to the track-based selection but is simpler.

Events with at least two oppositely charged τ candidates are selected. At least one of the candidates must be single-prong. The remainder of the event is forced to form two jets using the Durham clustering algorithm. Events which have more than one τ-pair candidate yield multiple $\tau^+\tau^-q\bar{q}$ combinations. A χ^2 is determined for each event combination with a kinematic consistency fit [19]. This fit requires energy-momentum conservation while keeping the four jet directions fixed. In the fit, the mass of the candidate τ jets is fixed to the nominal

11

τ lepton mass, and the energy resolution of the two non-τ jets is taken into account. The invariant mass of either the $\tau^+\tau^-$ or the $q\bar{q}$ pair is constrained to be compatible with the Z mass, depending on the channel. In addition, the non-τ jet momenta are constrained to be larger than 75% of the measured value. The combination with the lowest χ^2 is chosen and presented to the neural networks described below.

4.4.1   The $HZ \to H\tau^+\tau^-$ channel

To discriminate between $H\tau^+\tau^-$ and background events, a neural network is used with five input variables: the total missing transverse momentum of the event, the sum of the two τ jet isolation angles, the sum of the fitted transverse momenta of the τ jets with respect to their nearest hadronic jet, the kinematic consistency χ^2, and $(\eta_1 + \eta_2)$. The jet isolation angle definition for the second variable is the same as for the $H\ell^+\ell^-$ selection [3]. The last variable reflects the b-quark content of the two non-τ jets. Details of the neural network are discussed in the Appendix.
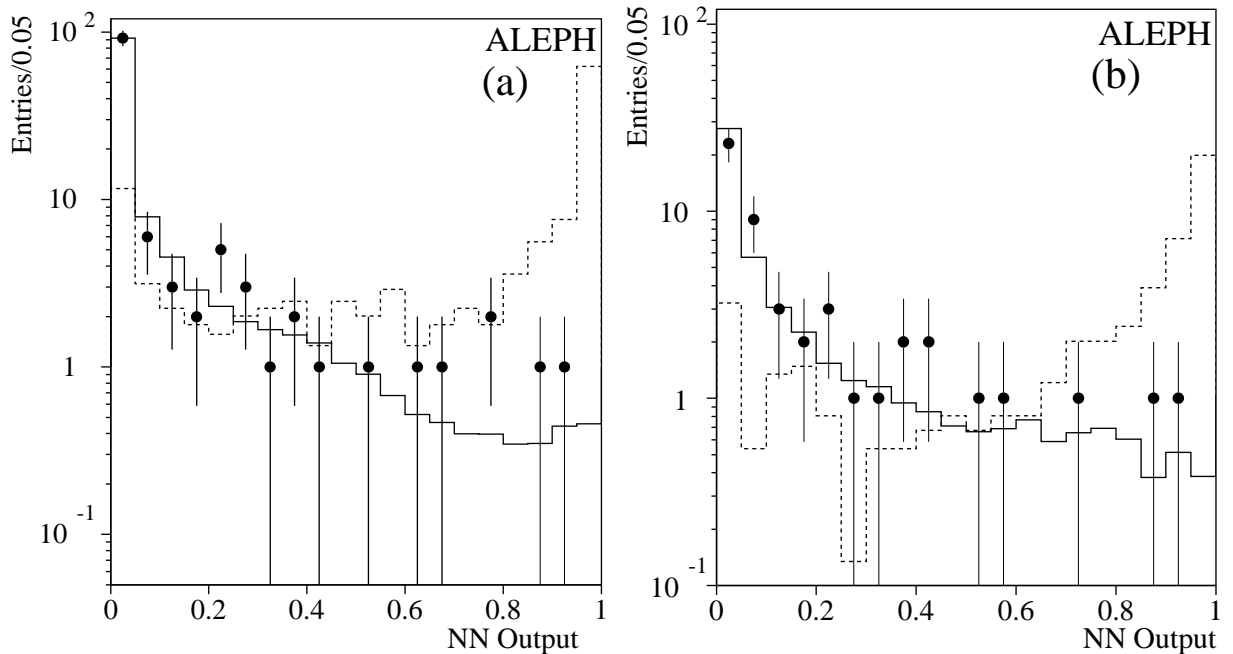

Figure 3: The distributions of the neural network outputs for (a) the $H\tau^+\tau^-$ channel and (b) the $\tau^+\tau^-q\bar{q}$ channel. The distributions are shown for the data (points), the total simulated background (solid histogram), and the reference signal sample (dashed histogram) after the preselection cuts. The signal distributions have an arbitrary normalization.

Figure 3a shows the response of the $H\tau^+\tau^-$ neural network in the data and in simulated signal and background events. The optimal point for this selection corresponds to neural network output values larger than 0.979.

4.4.2 The HZ → $\tau^+\tau^-$q$\bar{\text{q}}$ channel

A neural network is also used to select HZ → $\tau^+\tau^-$q$\bar{\text{q}}$ events. The input variables are identical to those described in the previous subsection except that the b-tagging variable is not used. This is a limiting factor in the performance of the selection. Figure 3b shows the neural network output in the data and simulated signal and background events. Events which have a neural network output larger than 0.980 are selected.

4.4.3 Systematic uncertainties

The main sources of systematic uncertainty in the final states with τ leptons are the reconstruction of the kinematic variables, the clustering of jets and the tagging of jets containing b quarks.

From a comparison of multihadronic events with an identified lepton, in the data and in simulated events, a slight discrepancy in the total transverse momentum distribution is observed which translates into an absolute uncertainty of 0.3% (0.2%) in the signal detection efficiency for the H$\tau^+\tau^-$ ($\tau^+\tau^-$q$\bar{\text{q}}$) channel. The effects from jet reconstruction are evaluated by smearing the reconstructed jet angles and energies according to the expected measurement errors. The systematic effect on the detection efficiency is 0.4% (0.1%) from the jet directions and 0.1% (0.1%) from the jet energies, in absolute terms. Uncertainties arising from the tagging of b-quark jets affect only the H$\tau^+\tau^-$ selection and are evaluated, as is described in Section 4, to be 0.9%. Therefore, total relative systematic uncertainties of 5.0% and 1.9% are respectively assigned to the H$\tau^+\tau^-$ and $\tau^+\tau^-$q$\bar{\text{q}}$ signal detection efficiencies.

5   Combined result

Seven events are selected in the data by the various selections, in agreement with the 7.2 events expected from all Standard Model background processes. Four of these events are selected in the four-jet final state. One event, selected by both the selection with cuts and the selection with neural networks, has a reconstructed Higgs boson mass of 71.5 GeV/c^2 while the other events selected with cuts (neural networks) only, have mass values of 76.1 and 85.0 GeV/c^2 (85.2 GeV/c^2). The other three candidate events are found in the leptonic final state, with masses of 67.0, 82.2, and 96.5 GeV/c^2. Figure 4 shows the reconstructed Higgs boson mass distribution for the selected events in all channels.

The result obtained when all sub-selections are combined is displayed in Fig. 5. This result includes the lower energy ALEPH data taken at LEP1 [20] and at $\sqrt{s} = 161, 170,$ and 172 GeV [3]. The lower energy data has an impact on the confidence level only for mass values lower than ~ 75 GeV/c^2.

The HZ searches exclude all Higgs boson masses below 88.0 GeV/c^2 at the 95% confidence level. The average limit expected in the absence of signal is 85.3 GeV/c^2. With this expected limit, the probability to observe a limit at least as high as 88.0 GeV/c^2 is 22%.

As explained in the previous sections, a number of possible systematic effects are studied and their impacts evaluated. The uncertainties related to the selection procedure and to the inadequacies of the Monte Carlo dominate, translating into uncertainties on the selection efficiencies ranging from $\sim 0.5\%$ to 7%, depending on the final state. Following the method of
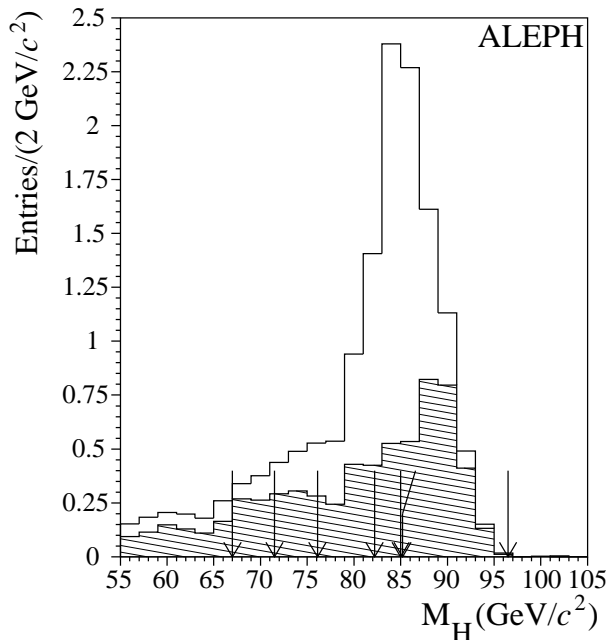
Figure 4: The distribution of the reconstructed Higgs boson mass of the selected events in all search channels. The histogram shows the expected distribution, with the contribution from background processes (shaded) and from the reference signal ($m_H = 85$ GeV/c^2), normalized to the collected data luminosity. The data events are indicated with arrows. The selected events do not have equal weights in the combination procedure but have been plotted here with unit weight for convenience.

Ref. [21], a small increase of the confidence level results, corresponding to a change in the mass limit of -0.1 GeV/c^2.

The mass of the Standard Model Higgs boson therefore exceeds 87.9 GeV/c^2 at the 95% confidence level. Had background subtraction been performed — with the same set of selection criteria and ignoring the related systematic uncertainties — a 95% confidence level limit of 88.3 GeV/c^2 would have been derived, with 88.3 GeV/c^2 expected.

6 Summary

A search for evidence of the production of Higgs bosons in e^+e^- collisions at centre-of-mass energies between 181 and 184 GeV has been performed with the ALEPH detector. The major event topologies have been covered: the leptonic and missing energy final states as well as the final states with four hadronic jets and those including τ leptons. The previously published search algorithms have been improved and new selections using artificial neural networks were introduced.

In the collected data sample, corresponding to a total of 57 pb^{-1}, seven events were selected, in agreement with 7.2 events expected from Standard Model background processes. From this observation, a 95% confidence level lower limit on the mass of the Higgs boson is set at 87.9 GeV/c^2. A similar result has been reported by the L3 experiment at LEP [22].
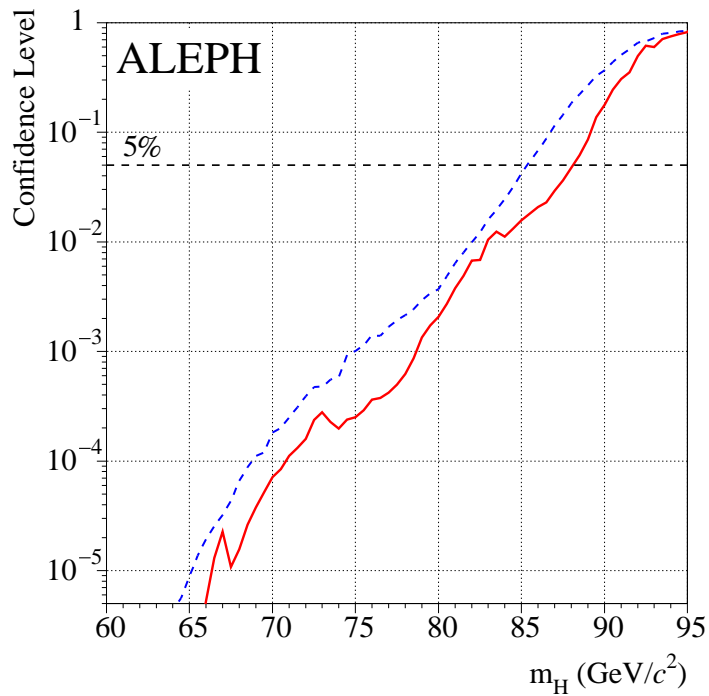
14

Figure 5: The observed (solid line) and expected (dashed line) confidence level curves after all channels are combined, using the 183 GeV data as well as the results obtained at lower energies.

Acknowledgements

Appendix

This appendix offers more details on the neural networks used for the H$\nu\bar{\nu}$, Hq$\bar{\text{q}}$, H$\tau^+\tau^-$, and $\tau^+\tau^-$q$\bar{\text{q}}$ selections. All of the neural networks are fully-connected multi-layer feed-forward networks trained with back-propagation algorithms using existing programs [23]. During an initial training phase, patterns composed of sets of discriminating variables are presented to the neural network, and the network weights are optimized to produce an output near one for signal patterns and near zero for background patterns.

The architecture and training details of the neural networks are summarized in Table 3. These parameters are chosen based upon optimal performance in Monte Carlo simulation. Each network is trained with Monte Carlo simulation of HZ signal samples as well as samples of background processes.

Table 3: A summary of the architecture and the HZ signal and background process training samples used for the neural networks described in the text.

Final State	Network Architecture	m_{H} in Signal Training Samples (GeV/c^2)	Background Training Samples
Hq$\bar{\text{q}}$ (anti-q$\bar{\text{q}}$)	22-10-10-1	70, 80, 85	q$\bar{\text{q}}(\gamma)$
Hq$\bar{\text{q}}$ (anti-W$^+$W$^-$)	14-12-10-2	80	W$^+$W$^-$
H$\nu\bar{\nu}$	11-20-3	80, 85	W$^+$W$^-$, q$\bar{\text{q}}(\gamma)$
H$\tau^+\tau^-$	5-10-1	80, 85, 90	W$^+$W$^-$, ZZ
$\tau^+\tau^-$q$\bar{\text{q}}$	4-10-1	80, 85, 90	W$^+$W$^-$, ZZ

For the four-jet final state, only the correct pairing in HZ $\rightarrow$ b$\bar{\text{b}}$q$\bar{\text{q}}$ events is presented to the neural network as the signal pattern during the training phase.

The input variables used for the anti-q$\bar{\text{q}}$ neural network in the Hq$\bar{\text{q}}$ channel are listed in Table 4.

The input variables used for the anti-W$^+$W$^-$ neural network in the Hq$\bar{\text{q}}$ channel are listed in Table 5. The event broadening is computed using the two event hemispheres defined by the plane perpendicular to the event thrust axis; the quantity B_{hemi} is computed for each hemisphere:

$$B_{\text{hemi}} = \frac{\sum_{i=1}^{N_{\text{tracks}}} \mid p_{\text{t}i} \mid}{\sum_{i=1}^{N_{\text{tracks}}} \mid p_i \mid} ,$$

where N_{tracks} is the number of tracks in the hemisphere, p_i is the momentum of the ith track, and $p_{\text{t}i}$ is the transverse momentum of the ith track with respect to the thrust axis. The event broadening B is the smaller of the two B_{hemi} values.

Table 4: The complete list of inputs to the anti-q$\bar{\mathrm{q}}$ neural network. The variables marked with † are common to the NN-based and cut-based selections and are described in Sections 4.3 and 4.3.1.

Variable	
1.	y_{34} †
2.	γ †
3.	m_{12} †
4.	$\min(\eta_3, \eta_4)$ †
5.	$(1 - \eta_3)(1 - \eta_4)$ †
6.	$\sum_{i=1}^{4} \eta_i$ †
7.	Θ †
8.	$\langle \mathcal{M} \rangle$, average four-jet QCD matrix element.
9–10.	Boosted aplanarity of Z candidate jets.
11–12.	Boosted sphericity of Z candidate jets.
13–14.	Multiplicity of tracks with rapidity larger than 1.6, in the Z candidate jets.
15.	$\min(\theta_{ij})$, lowest interjet angle.
16.	$\cos\theta_{p\!\!\!/}$, cosine of the polar angle of the event missing momentum vector.
17.	$\min(m_{ij} + m_{kl})$, lowest di-jet mass sum.
18–19.	$m_{\min}, m_{\min 2}$, the two lowest jet masses.
20–21.	$E_{\min}, E_{\min 2}$, the two lowest jet energies.
22.	$E_{\max}$, largest jet energy.

Table 5: The complete list of inputs to the anti-W$^+$W$^-$ neural network. The variables marked with † are common to the NN-based and cut-based selections and are described in Sections 4.3 and 4.3.1.

Variable	
1.	y_{34} †
2.	γ †
3.	m_{12} †
4–5.	$\min(\eta_3, \eta_4), \max(\eta_3, \eta_4)$ †
6.	$(1 - \eta_3)(1 - \eta_4)$ †
7.	$\sum_{i=1}^{4} \eta_i$ †
8–9.	$\min(\eta_1, \eta_2), \max(\eta_1, \eta_2)$
10–11.	$\min(\mu_3, \mu_4), \max(\mu_3, \mu_4)$
12.	B, event broadening.
13.	$E_{\min}$, lowest jet energy.
14.	$\min(m_{ij})$, lowest di-jet mass.

References

[1] M. Grünewald, *Combined Analysis of Electroweak Precision Results*, talk presented at the ICHEP, Vancouver, August 1998, to appear in the proceedings.

[2] For reviews see:
J.F. Gunion, H.E. Haber, G. Kane and S. Dawson, *The Higgs Hunter's Guide* (Addison-Wesley, 1990) and references therein.
P.J. Franzini et al., in *Z Physics at LEP 1*, Eds. G. Altarelli, R. Kleiss and C. Verzegnassi, CERN 89-08 (1989).
M. Carena and P. Zerwas (Conveners) et al., *"Higgs Physics"*, in *Physics at LEP 2*, Eds. G. Altarelli, T. Sjöstrand, and F. Zwirner, CERN 96-01 (1996) 351.

[3] ALEPH Collaboration, *Search for the Standard Model Higgs boson in e^+e^- collisions at $\sqrt{s}$ =161, 170 and 172 GeV*, Phys. Lett. **B412** (1997) 155.

[4] DELPHI Collaboration, *Search for neutral and charged Higgs bosons in e^+e^- collisions at $\sqrt{s} = 161$ GeV and 172 GeV*, E. Phys. J. **C2** (1998) 1.

[5] L3 Collaboration, *Search for the Standard Model Higgs boson in e^+e^- interactions at 161 GeV $< \sqrt{s} < 172$ GeV*, Phys. Lett. **B411** (1997) 373.

[6] OPAL Collaboration, *Search for the Standard Model Higgs boson in e^+e^- collisions at $\sqrt{s} = 161$–172 GeV*, E. Phys. J. **C1** (1998) 425.

[7] ALEPH Collaboration, *Search for the neutral Higgs bosons of the MSSM in e^+e^- collisions at $\sqrt{s}$ from 130 to 172 GeV*, Phys. Lett. **B412** (1997) 173.

[8] ALEPH Collaboration, *ALEPH: A detector for electron-positron annihilations at LEP*, Nucl. Instrum. Methods **A294** (1990) 121.

[9] ALEPH Collaboration, *Performance of the ALEPH detector at LEP*, Nucl. Instrum. Methods **A360** (1995) 481.

[10] D. Creanza et al., *Construction and Performance of the New ALEPH Vertex Detector*, to appear in the Proceedings of the Conference on Advanced Technology and Particle Physics, Como, Italy, 7–11, October 1996.

[11] P. Janot and F. Le Diberder, *Optimally combined confidence limits*, Nucl. Instrum. Methods **A411** (1998) 449.

[12] See for instance:
C. Peterson and T. Rögnvaldsson, *An Introduction to Artificial Neural Networks, 1991 CERN School of Computing* (Ed. C. Verkerk) 113;
L. Lönnblad, C. Peterson, and T. Rögnvaldsson, *Pattern recognition in high energy physics with artificial neural networks — JETNET 2.0*, Comput. Phys. Commun. **70** (1992) 167;
S.R. Amendolia, *Neural Networks, 1993 CERN School of Computing* (Eds. C.E. Vandoni and C. Verkerk) 1.

[13] P. Janot, *The HZHA generator*, in G. Altarelli, T. Sjöstrand, F. Zwirner (Editors), Physics at LEP2, CERN 96-01, 1996, Vol. 2, 309.

[14] C. Peterson, D. Schlatter, I. Schmitt, and P. M. Zerwas, *Scaling violations in inclusive e^+e^- annihilation spectra*, Phys. Rev. **D27** (1983) 105.

[15] ALEPH Collaboration, *Measurement of the effective b Quark Fragmentation Function at the Z Resonance*, Phys. Lett. **B357** (1995) 699;
ALEPH Collaboration, *Inclusive Heavy Flavour Lifetime and Mixing Measurements at ALEPH*, paper #596 submitted to the EPS-HEP97 Conference, Jerusalem, 19–26 August 1997.

[16] W. J. Stirling, *Hard QCD Working Group—Theory Summary*, J. Phys. **G17** (1991) 1567.

[17] D. Danckaert et al., *Four-jet Production in e^+e^- Annihilation*, Phys. Lett. **B114** (1982) 203.

[18] ALEPH Collaboration, *A measurement of R_b using mutually exclusive tags*, Phys. Lett. **B401** (1997) 163.

[19] ALEPH Collaboration, *Searches for the Neutral Higgs bosons of the MSSM in e^+e^- collisions at Centre-of-Mass Energies of 181–184 GeV*, CERN-EP/98-145 (to appear in Phys. Lett. B).

[20] ALEPH Collaboration, *Mass Limit for the Standard Model Higgs Boson with the full LEP1 ALEPH data sample*, Phys. Lett. **B384** (1996) 427.

[21] R.D. Cousins and V.L. Highland, *Incorporating systematic uncertainties into an upper limit*, Nucl. Instrum. Methods **A320** (1992) 331.

[22] L3 Collaboration, *Search for the Standard Model Higgs Boson in e^+e^- Interactions at $\sqrt{s} = 183$ GeV*, CERN-EP/98-052 (to appear in Phys. Lett. B).

[23] A. Zell et al., *SNNS - Stuttgart Neural Network Simulator User Manual, Version 4.0*, University of Stuttgart, Institute for Parallel and Distributed High Performance Computing (IPVR), Department of Computer Science, Report 6/95, 1995;
L. Lönnblad, C. Peterson, and T. Rögnvaldsson, *JETNET 3.0 : A Versatile Artificial Neural Network Package*, CERN-TH 7135/94 (1994);
J. Proriol, *Multi-modular Neural Networks for the Classification of e^+e^- Hadronic Events*, Nucl. Instrum. Methods **A337** (1994) 566.